PCCP

ROYAL SOCIETY OF CHEMISTRY

PAPER

View Article Online
View Journal | View Issue

Check for updates

Cite this: *Phys. Chem. Chem. Phys.*, 2024, **26**, 16296

Unexpected concentration dependence of the mass accommodation coefficient of water on aqueous triethylene glycol droplets†

Michael J. Gleichweit, Mercede Azizbaig Mohajer, Dominique P. Borgeaud dit Avocat, Matúš E. Divéky, Grégory David and Ruth Signorell*

Received 5th March 2024,
Accepted 15th May 2024

DOI: 10.1039/d4cp00966e

rsc.li/pccp

The mass accommodation coefficient α_M of water on aqueous triethylene glycol droplets was determined for water mole fractions in the range x_{mol} = 0.1–0.93 and temperatures between 21 and 26 °C from modulated Mie scattering measurement on single optically-trapped droplets in combination with a kinetic multilayer model. α_M reaches minimum values around 0.005 at a critical water concentration of x_{mol} = 0.38, and increases with decreasing water content to a value of $\approx$0.1 for almost pure triethylene glycol droplets, essentially independent of the temperature. Above x_{mol} = 0.38, α_M first increases with increasing water content and then stabilises at a value of $\approx$0.1 at the lowest temperatures, while at the highest temperature its value remains around 0.005. We analysed the unexpected concentration and temperature dependence with a previously proposed two-step model for mass accommodation which provides concentration and temperature-dependent activation enthalpies and entropies. We suggest that the unexpected minimum in α_M at intermediate water concentrations might arise from a more or less saturated hydrogen-bond network that forms at the droplet surface.

1 Introduction

Introduced as a concept already by Maxwell in 1859,[1] the mass accommodation coefficient (α_M) still plays a key role in the quantitative description of mass transport from the gas to the condensed phase (liquid, solid).[2–5] It represents the fraction of gas phase molecules that remain in the condensed phase after colliding with the surface ($0 \leq \alpha_M \leq 1$).

$$\alpha_M = \frac{\text{No. of molecules colliding with the surface}}{\text{No. of molecules incorporated into the condensed phase}} \quad (1)$$

Even though many different experimental approaches have been invented to measure α_M, the determination of accurate experimental accommodation coefficients has been challenging.[2,4–7] The reasons are diverse, mainly concerning various experimental but also conceptual aspects.[5,7–10] Theoretical approaches to retrieve α_M, such as molecular dynamics simulations, provide an alternative option to the experiment.[11–18] But they have their own challenges, and direct comparison with experimental data remains demanding.

This is partly because in theoretical studies the mass accommodation process has often been divided into a surface accommodation step and a subsequent transfer to bulk. However, distinguishing the two steps is rarely possible in experiments.[7] The first step is described by an accommodation coefficient α_S defined as "the number of gas phase molecules accommodated at the surface divided by the total number of molecules colliding with the surface".[5] The bulk accommodation coefficient α_B is "the number of molecules incorporated into the particle bulk divided by the total number of molecules colliding with the surface".[5] In our experiment, we cannot distinguish between surface accommodated molecules and bulk accommodated molecules. Therefore, we use the symbol α_M for the accommodation coefficient determined in our experiments (see Section 3). Assuming that most molecules that accommodate at the surface either desorb or are subsequently accommodated into the bulk, α_M would approach α_B as defined above.[5,19] Another coefficient that is closely related to α_M is the uptake coefficient γ. It describes the ratio of the number of molecules removed from the gas phase divided by the total number of molecules colliding with the surface.[5,19] In the absence of chemical reactions, if diffusion is fast and if the system stays close to equilibrium,[3,5,7,20–22] γ is

---

Department of Chemistry and Applied Biosciences, ETH Zurich, CH-8093 Zurich, Switzerland. E-mail: ruth.signorell@phys.chem.ethz.ch

† Electronic supplementary information (ESI) available. See DOI: **https://doi.org/10.1039/d4cp00966e**

equal to α_M.[5,23] Our experiment closely appraoches these conditions.

As a consequence, consensus does not even exist on the value of the accommodation coefficient for water vapour on liquid water, *i.e.* for one of the most important systems.[4,24–28] Over the last two decades there has been increasing evidence that the value for water on water might be larger than 0.6, possibly close to unity.[9,26,27,29] Because of the omnipresence of water, water-containing multi-component systems are of particular interest.[2,3,7,22,30–35] The knowledge of α_M for these systems is relevant for cloud activation by atmospheric aerosols and cloud formation, and questions concerning the delivery of aerosolised pharmaceutics to the lungs and their effectiveness. The accommodation coefficient of multi-component systems does not only vary with the composition of the condensed phase but also with temperature. For surface-active and water-immiscible compounds, a non-trivial dependence of α_M on temperature and composition is expected, similar to what has been reported for the temperature dependence in ref. 33, 34 and 36.

Here, we report experimental values of α_M for aqueous triethylene glycol (TREG) droplets over a wide concentration range from essentially pure TREG droplets (<2% water by volume) to water-rich droplets (<60% water by volume) at temperatures between 21 °C and 26 °C. Note that although these droplets are rich in water, they are not comparable to almost pure water droplets. TREG is a colourless, odourless, viscous liquid that is commonly used for humidity control of room air, air and surface disinfection, dehydration during natural gas production, as working fluid in fog machines and for moisture control of tobacco products.[37–41] For the determination of α_M, we combined our newly developed Photothermal Single-Particle Spectroscopy (PSPS)[7,30,42–46] with our recently developed multilayer heat and mass flux model for photoacoustic spectroscopy on single aerosol particles (MHM-PA).[47]

PSPS consists of an optical trap (not shown in Fig. 1) that immobilises a single droplet in a gas environment of controlled gas composition, relative humidity, pressure and temperature. Once trapped, the droplet and gas phase are in equilibrium. A small but fast, periodic perturbation is then applied to the droplet by excitation with a sinusoidally intensity-modulated infrared (IR) laser that is absorbed by the droplet. The light energy deposited in the droplet results in periodic heat (thermal energy) and mass exchange (condensation and evaporation) between droplet and surrounding gas phase (Fig. 1). Heat flux is exchange of thermal energy between the particle surface and ambient gas phase molecules through ballistic collisions. Mass flux describes the transport of molecules across the interface, with an energy transfer characterised by the associated latent heat. This is accompanied by periodic changes of the droplet temperature ($T(t)$) and the droplet radius ($r(t)$) caused by water evaporation and condensation, and by thermal expansion and contraction. For aqueous TREG droplets, only water contributes to the mass exchange because of the very low vapour pressure of TREG (<1 Pa). The change in temperature and composition (evaporation and condensation, here given by the water concentration $C_w(t)$) also results in a periodic change of the refractive index ($n(t)$).

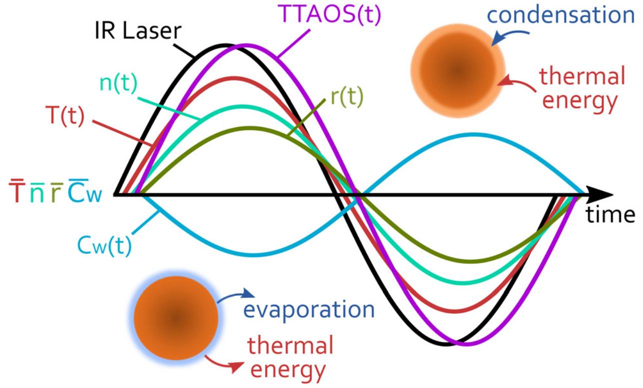

Fig. 1 Illustration of how different physical quantities of a single droplet oscillate around their average values (symbols with bar) during a photothermal excitation cycle. The IR laser trace illustrates the temporal evolution of the energy deposition into the droplet. The temperature $T(t)$, complex refractive index $n(t)$, particle radius $r(t)$, and water concentration $C_w(t)$ oscillate with the same frequency, but show an individual phase delay. The recorded scattering intensity TTAOS(t) for each point in time is dictated by the refractive index and particle radius, which in turn are functions of temperature and water concentration.

In our previous studies using PSPS, we have shown that α_M can be retrieved simultaneously from the measurement of three independent signals, which are the photoacoustic amplitude (PAA), the photoacoustic phase (PAP) and modulated Mie scattering (MMS).[43,45] The PAA and PAP are recorded with a microphone or other acoustic transducers,[42] while MMS relies on optical detection, where the periodic change in the droplet size and refractive index is measured by collecting the light (usually from the trapping laser) elastically scattered by the droplet. In the present study, we only employed MMS because it had the best signal quality and, compared with PA, it is a calibration free method (see Section 2.2). Important advantages of PSPS are its high sensitivity and the fact that the measurements are performed under near equilibrium conditions (small perturbation). In addition, the single droplet approach circumvents issues with unwanted ensemble averaging, and it guarantees optimal control of droplet properties (size, composition, temperature) and environmental conditions.

TREG and water are miscible. In contrast to multi-component systems containing surface-active or water-immiscible compounds,[33,34] one would rather expect to observe a monotonic concentration and temperature behaviour for α_M. However, as we show in this study this is not the case for the concentration dependence, which actually exhibits an unexpected minimum in α_M at intermediate water concentrations. The temperature dependence of droplets with intermediate to high water content, by contrast, follows the systematic trend that was expected based on our previous study of water accommodation on aqueous tetraethylene glycol (TEG) droplets;[43,45] *i.e.* a systematic decrease of α_M with increasing temperature. We analyse the observed trends in α_M with the two-step model proposed in previous studies by Nathanson *et al.* and

Davidovits *et al.*[20,48] which provides values for the activation Gibbs free energy ΔG_{obs}, and the activation enthalpy ΔH_{obs} and entropy ΔS_{obs}.

2 Experimental

2.1 Single droplet optical trap

A sketch of the experimental setup is shown in Fig. 2. Single aqueous triethylene glycol ($C_6H_{14}O_4$) droplets were immobilised in a humidified nitrogen atmosphere by counter-propagating optical tweezers (CPT). The CPT optical trap was built from a continuous wave laser (trapping laser) with a wavelength of 532 nm (CWL, Laser Quantum Opus 532, 220 mW), which was protected against unwanted backreflections by an optical isolator (OI, Thorlabs IO-5-532-HP). The trapping laser passed through an electro-optic modulator (EOM, Conoptics 350-50-01) that enabled dynamic rotation of its polarisation state, before being expanded to a diameter of 7.4 mm using a beam expander (BE, Edmund Optics #37-053). The single beam passed through a half-wave plate (HWP) before being split into two beams of orthogonal polarisation by a polarisation beamsplitter cube (PBS). The HWP after the EOM was used to fine-tune the neutral point of the power-splitting to create a stable counter-propagating trap. Each of the two beams was directed onto an aspherical lens (AL, 75 mm, Thorlabs ASL10142), which focused them in the centre of a custom-built photoacoustic trapping cell (TC). The benefit of this CPT setup is a tight droplet confinement perpendicular to the directions of the trapping beams combined with long working distances. To also maintain a high confinement of the droplets along the trapping laser directions, we implemented a feedback system in which the particle's position is continuously monitored by projecting light elastically scattered by the droplet onto a position sensitive photodiode (PSD, lateral effect sensor, Thorlabs PDP90A; Fig. 2 right). The PSD sensor was connected to a proportional-integral-derivative controller (PID, Thorlabs KPA101), which regulated the voltage applied to the EOM and thus the polarisation state of the trapping beam before passing the PBS. This closed-loop control circuit rapidly adjusted the power ratio of the two counter-propagating beams at a time scale of up to 20 kHz (limited by the PID controller). It thereby applies static and dynamic corrections to the particle's position and ensures stable trapping during the measurement.

The TC is described in more detail in ref. 42. It is made of stainless steel and holds a relative humidity and temperature sensor (Sensirion SHT35). It can also be used for photoacoustic measurements at a resonance frequency of 3540 Hz.[49] Aqueous TREG droplets generated by a medical nebuliser were trapped by the CPT. The relative humidity (RH), and with this the composition of the particle,[50,51] was set by a humidified nitrogen gas flow of 30 sccm. The RH was controlled by a PID controller implemented in LabVIEW, which regulates the mixing ratio of a dry and a humidified nitrogen gas flow prior to the cell inlet.

2.2 Modulated Mie scattering

The particle radius r and α_M were retrieved from the trapping laser light that was elastically scattered by the droplet using Mie theory.[52] The light scattering patterns depend on r and on the refractive index (droplet composition). The elastically scattered light was collected over an angular range of 49.0° around a scattering angle of 90° (Fig. 3) using a microscope objective (Mitutoyo, M Plan Apo 20×, slightly de-collimated operation). The collected scattered light was divided up by non-polarising beam splitter cubes (BS) (Fig. 2, right), and directed onto a photodiode (PD, Hamamatsu S2506-02) for the determination of r and α_M, onto the CMOS camera (CM) for observation of the

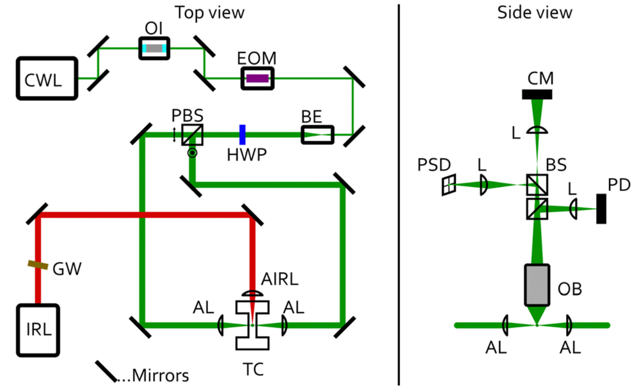

Fig. 2 Schematic of the experimental setup. Top view (left). CWL: continuous wave trapping laser, λ = 532 nm; IRL: modulated infrared laser, λ = 9456 nm; GW: Germanium Longpass filter; OI: optical isolator; EOM: electro-optical modulator; BE: beam expander; HWP: half-wave plate; PBS: polarising beam splitter cube; AL: aspheric trapping lenses; AIRL: aspheric infrared lens, CaF_2; TC: trapping cell. Side view (right). OB: objective, 20×, NA = 0.42; BS: beam splitter cube; L: spherical lenses; PD: photodiode; PSD: position sensitive detector; CM: CMOS camera.

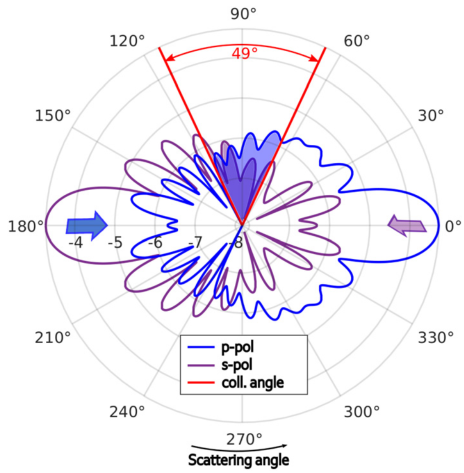

Fig. 3 Sketch of the angle-dependence of the light from the trapping laser scattered by a single droplet. The blue and purple traces outline the angle dependent scattering intensity for the s- and p-polarised trapping beams, respectively. The correspondingly coloured blue and purple arrows indicate the propagation directions of the two beams. The red lines indicate the collected angular range of the microscope objective used to record TTAOS and MMS (see text).

particle in the trap,[53] and onto the PSD for feedback stabilisation (see above).

Fig. 3 illustrates the angle-dependent scattering intensity of a droplet for cross-polarised, counter-propagating optical tweezers, viewed in the same plane as in Fig. 2 (right). The red lines indicate the collection angle of the microscope objective. The blue and purple trace illustrate the scattering intensity profiles of the p- and s-polarised trapping beams, respectively. The PD records the integrals over the collected angular range, visualised by the corresponding blue- and purple-shaded areas.

To determine α_M, a small fast periodic (3540 Hz) perturbation was induced in the droplet by exposing the droplet to an intensity modulated infrared (IR) laser (IRL, AdTech Optics, λ = 9456 nm, TEC controlled), which was focused onto the trapping position using a ZnSe lens (AIRL, 75.0 mm, Thorlabs, LA7660-G)(Fig. 2).[30] An angled Germanium Longpass filter (GW, Edmund Optics, #36-151) protects the IR laser against unwanted reflections. The IR light was absorbed by TREG and resulted in periodic changes of the droplet temperature and concentration (and therefore the refractive index), and the droplet radius. These changes are the result of periodic heat (expansion/contraction) and mass flux (evaporation/condensation of water) away and towards the droplet (Fig. 1). The very small changes in refractive index ($\Delta n_r < 0.06$) and radius ($\Delta r <$ 2 nm) manifested themselves as periodic changes in the scattering patterns (Fig. 3), and hence characteristic changes of the recorded PD signal. Demodulating the PD signal at the modulation frequency of the IR laser yields a complex signal $\text{MMS} = X + iY$, referred to as modulated Mie scattering (MMS). We refer to the absolute value of this signal as the experimental MMS amplitude $\text{MMS}_A^{\text{exp}} = \sqrt{X^2 + Y^2}$ (Fig. 4(a) and (b), blue trace). The phase shift of the MMS signal in our experiments is measured with respect to the IR laser, and is referred to as the experimental MMS phase $\text{MMS}_\phi^{\text{exp}} = \text{atan2}(Y,X)$ (Fig. 4(b), red trace).[30]

Aqueous TREG droplets evaporate very slowly on a time scale (minutes to hours) much slower than the modulation period (~250 μs) of the IR laser; *i.e.* the decrease of the droplet size caused by slow evaporation is negligible for the MMS measurements. The slow shrinking of the droplets over time enabled the determination of the average absolute droplet radius $\bar{r}$ and normalisation of the MMS signals (eqn (2)). The droplet shrinking is contained in the DC signal of the PD, which is referred to as Total Two-dimensional Angular Optical Scattering, $\text{TTAOS}^{\text{exp}}$.[53] Fig. 5 (brown trace) shows the theoretical TTAOS signal as a function of the average droplet radius $\bar{r}$ and the average real part of the refractive index $\bar{n}_r$ (droplet composition). $\bar{r}$ was determined from the analysis of Mie resonances (maxima), resulting in an uncertainty in $\bar{r}$ of less than ±2 nm for sizes in the sub-micrometre to micrometre range.[53] The size of the droplets was also exploited to adjust the average droplet temperatures $\bar{T}$ between 21 °C and 26 °C. Larger droplets have a higher IR absorption cross section and a reduced surface-to-volume ratio compared with smaller droplets. As a result, larger droplets equilibrate at a higher $\bar{T}$ during modulated IR excitation.

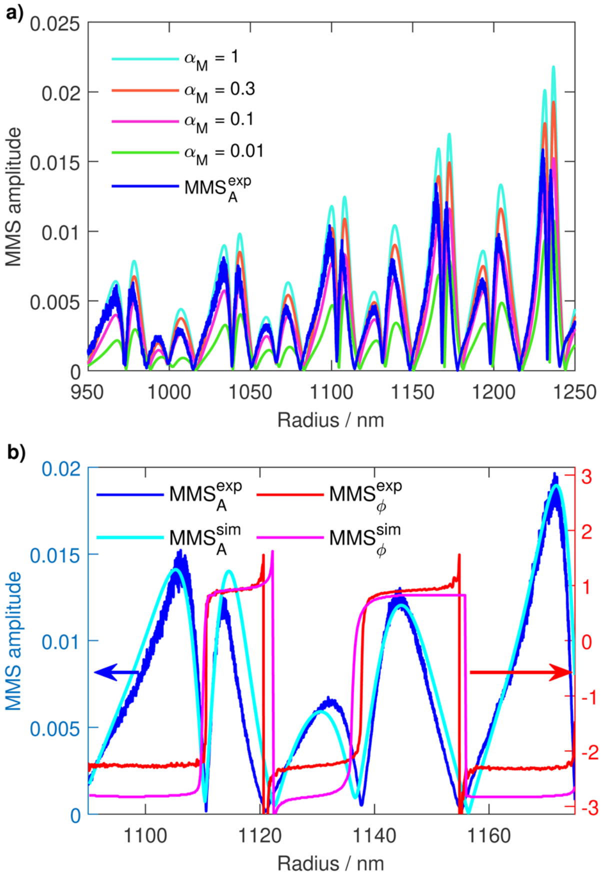

Fig. 4 Comparison between experimental and simulated MMS data. (a) Comparison of the experimental MMS amplitude with simulated MMS amplitudes for four different α_M between 0.01–1 at a RH of 50%. (b) MMS amplitudes and phases as a function of the droplet radius for a measurement at a RH of 68% and for α_M = 0.1389. Both the simulated MMS amplitude and phase show very good agreement with the experimental data.

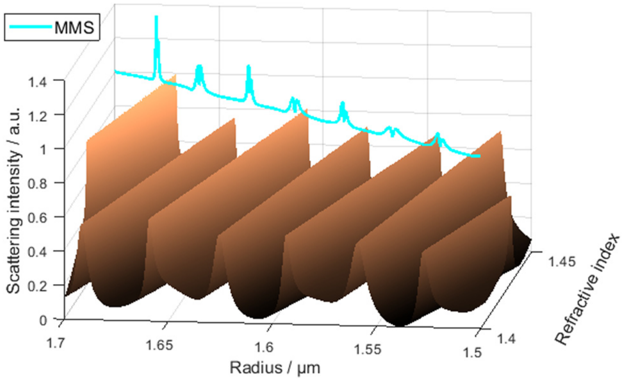

Fig. 5 Calculated scattering intensity (TTAOS) for a range of typical droplet radii and refractive indices. The light-blue line illustrates the calculated MMS signal when a droplet shrinks from 1.7 to 1.5 μm.

The signal from the PD was recorded and evaluated by a lock-in amplifier (Zürich Instruments MFLI, 500 kHz), which also controlled the IR laser modulation. This lock-in amplifier provided the amplitude and phase response at the IR modulation frequency (MMS signals) as well as the $\mathrm{TTAOS^{exp}}$ signal. To compare the $\mathrm{MMS_A^{exp}}$ with the simulated amplitude $\mathrm{MMS_A^{sim,norm}}$ (eqn (9), section Modelling), the former was normalised by the total experimental scattering intensity $\mathrm{TTAOS^{exp}}$.

$$\mathrm{MMS_A^{exp,norm}} = \frac{\mathrm{MMS_A^{exp}}}{\mathrm{TTAOS^{exp}}} \tag{2}$$

Eqn (2) represents a dimensionless MMS amplitude that can be directly compared with simulations because it is independent of the power from the trapping laser beam of which the elastically scattered light is collected.

In principle, the modulation frequency of the IR laser can be chosen arbitrarily. However, there are certain physical limitations to consider. To be able to observe processes such as evaporation and condensation through damping of the amplitude and the phase delay, the period of the driving laser $1/\omega$ and the relaxation time τ of the system should be of roughly the same order of magnitude:

$$\omega \cdot \tau \approx 1 \tag{3}$$

Depending on the choice of RH and r, our experiments operated in the range $\omega \cdot \tau = 0.3$–4 ($15\ \mu\mathrm{s} < \tau < 180\ \mu\mathrm{s}$).

3 Modelling

For the simulation of the MMS signals, we combined Mie theory for light scattering with Fourier's law of thermal conduction and Fick's first law of diffusion to describe heat and mass flux, respectively. External fluxes according to eqn (4) and (5) (heat and water mass exchange of the liquid surface of the particles with the surrounding gas phase) and internal diffusion of heat and water according to eqn (7) were calculated as a function of time t during photothermal cycles using our recently reported multi-layer heat and mass transfer model MHM-PA.[47] MHM-PA is a numerical approach to solve Fick's first law of diffusion, and hence allows us to simulate heat and mass flux away from and towards the droplet and the temporal evolution of the water concentration and temperature inside the droplet at conditions close to equilibrium. In contrast to the multi-layer model reported by Shiraiwa *et al.*,[21,54] we do neither assume a sorption layer nor a quasi-static surface layer to model the cyclic heat and water exchange with the ambient gas phase. Instead, we use eqn (4) and (5) based on the work by Kulmala *et al.*, Murphy and Winkler *et al.*[55–57] This is conceptually similar to the resistor model often used. In our model, the surface is not at strict equilibrium with the ambient gas phase. In fact, we assume that during a cycle, there is a slight difference (ΔT in eqn (4) and (5)) between the temperature of the surrounding gas phase and the temperature at the droplet surface ($\bar{T} + \Delta T$).[7,49]

The heat flux ΔQ away from or towards the droplet during a photothermal cycle can be expressed as:

$$\Delta Q = 4\pi r \beta_T K(\bar{T}) \Delta T \tag{4}$$

r is the particle radius, β_T is the transition correction factor for heat transfer, $K(T)$ the heat conductivity of the surrounding gas, $\bar{T}$ the average particle temperature and ΔT is the maximum change of the temperature at the droplet's surface from $\bar{T}$ during a photothermal cycle. The mass flux ΔI of water molecules away from or toward the droplet surface is given by Fick's law combined with the Clausius–Clapeyron equation, assuming an ideal gas:

$$\Delta I = 4\pi r \beta_M D_M \frac{M_v p_v(\bar{T})}{R} \left[\frac{LM_v}{R\bar{T}} - 1 \right] \frac{\Delta T}{(\bar{T} + \Delta T)^2} \tag{5}$$

β_M is the transition correction factor for mass transfer, D_M is the diffusion coefficient, M_v is the molar mass of the evaporating/condensing species (water), $p_v(T)$ is the water vapour pressure at temperature T, L is the latent heat, and R is the universal gas constant. Based on the original work of Fuchs and Sutugin,[58] the transition correction factors for heat transfer i = T and mass transfer i = M can be expressed as:

$$\beta_i = \frac{1 + \mathrm{Kn_i}}{1 + \left(\frac{4}{3\alpha_i} + 0.377 \right) \mathrm{Kn} + \frac{4}{3\alpha_i} \mathrm{Kn_i}^2}, \quad \mathrm{i} = T, M \tag{6}$$

where $\mathrm{Kn_i}$ are the Knudsen numbers $\mathrm{Kn_T} = \lambda_{N_2} r^{-1}$ and $\mathrm{Kn_M} = \lambda_v r^{-1}$, which depend on the mean free path of the ambient gas molecules λ_{N_2} and water vapour molecules λ_v, respectively. α_T is the thermal accommodation coefficient and α_M is the mass accommodation coefficient; *i.e.* the quantity to be determined in this work. α_T is generally assumed to be close to or equal to 1.[56,57,59,60] Consistently with our previous work and other authors, we set $\alpha_T = 0.97$.[47,49,56]

The MHM-PA model does not explicitly treat surface and bulk mass accommodation separately. This is consistent with the fact that the experimental data do not provide any information on the individual processes, but only on the entire process. Consistent with the experimental information we have, we thus incorporate the mass transfer process into the model *via* the transition regime correction factor β_M (eqn (6)).[7,47,55–57] This approach works well for the measurements presented here because TREG particles even when they are dry remain moderately viscous (< 0.049 Pa s[50]). Hence the viscosity is not limiting the mass accommodation of water in our droplets, unlike what has been observed with highly viscous particles.[22,61] For highly viscous or reactive particles, a sorption layer or quasi-static surface layer would need to be implemented in the model.

During a photothermal cycle, small gradients in the temperature and water concentration establish inside the droplet. The temporal evolution of these gradients can be described by Fick's first law of diffusion:

$$\vec{F} = D\vec{\nabla}C \tag{7}$$

Here, $\vec{F}$ is the heat or mass flux vector, D is the corresponding heat or mass diffusion coefficient, $\vec{\nabla}$ is the gradient operator, and C is the temperature or the water concentration.

The MHM-PA model divides the droplet into a discrete number of radial layers. Each layer has a particular time-dependent temperature, water concentration (refractive index) and volume. The flux F of either heat or mass from one layer i to the adjacent layers $i \pm 1$ can be expressed as

$$F_{i,i\pm1}(t) = k(T,x_{\mathrm{mol}})\delta C_{\mathrm{w},i,i\pm1}(t), \tag{8}$$

where k are transport velocities for either heat or mass that depend on T and the water mole fraction x_{mol}. They depend on the thermal diffusivity or mutual diffusion coefficients, respectively, which in turn depend on temperature T and water concentration C_{w}. $\delta C_{\mathrm{w},i,i\pm1}(t)$ are the gradients in water concentration or temperature between adjacent layers. The number of layers was retained during the simulation. Because the droplet slightly expands and contracts during the cycles, the thickness of the layers must also slightly shrink or grow. For water-TREG droplet simulations at a modulation frequency of 3540 Hz, simulation time steps of 6 ns and layer thicknesses between 46–50 nm were used. We also performed simulations with layers that are five times thinner. These simulations showed no change of the results, confirming convergence with respect to the layer thickness (see Fig. S1, ESI†). The simulation parameters used here are listed in the ESI,† and more detailed information about the simulations are given in ref. 47.

An MHM-PA simulation provides the temporal evolution of r, T, n and C_{w} during a cycle, which is schematically illustrated in Fig. 1. From these quantities, the time-dependent scattering intensity TTAOS(t) (Fig. 1, purple trace) was calculated for all experimental $\bar{r}$ and RH. Fig. 1 also schematically shows that r, T, n and C_{w} have individual phase delays. Thus, the resulting TTAOS signal is no longer strictly sinusoidal as it contains small higher frequency components. In the experiment, the lock-in amplifier filters out all unwanted frequency components. To account for this, the simulated signals were also digitally filtered, which provides TTAOS(t) at the modulation frequency. The MMS amplitude $\mathrm{MMS}_{\mathrm{A}}^{\mathrm{sim,norm}}$ was then calculated according to eqn (9). This procedure can be considered equivalent to the amplitude-demodulation during the experiment.

$$\mathrm{MMS}_{\mathrm{A}}^{\mathrm{sim,norm}}(\bar{r}) = \frac{|\max(\mathrm{TTAOS}(t)) - \min(\mathrm{TTAOS}(t))|}{2\sqrt{2}\overline{\mathrm{TTAOS}}} \tag{9}$$

$\bar{r}$ is the average particle radius, $\overline{\mathrm{TTAOS}}$ the average scattering intensity over a full excitation cycle, and max(TTAOS(t)) and min(TTAOS(t)) are the maximal and minimal scattering intensity within one cycle, respectively. Because the lock-in amplifier provides root-mean-square data for a sinusoidal signal and the simulations determine peak-peak amplitudes, an additional factor of $2\sqrt{2}$ is necessary to compare the MMS simulations with the experimental MMS signal. Eqn (9) normalises the calculated MMS amplitude by the average scattering intensity ($\overline{\mathrm{TTAOS}}$). After normalisation, this calculated signal is directly comparable with the normalised experimental MMS signal amplitude (eqn (2)), without any calibration.

The MMS phase, MMS_{ϕ}, was calculated from the time difference between the IR laser maximum $t_{\mathrm{IR,max}}$, and the first maximum in TTAOS(t), $t_{\mathrm{MMS,max}}$, according to eqn (10):

$$\mathrm{MMS}_{\phi}^{\mathrm{sim}}(\bar{r}) = 2\pi\frac{t_{\mathrm{IR,max}} - t_{\mathrm{MMS,max}}}{t_{\mathrm{mod}}} \tag{10}$$

t_{mod} is the duration of one modulation cycle. However, the simulated MMS phase cannot be compared with the experiment in quantitative terms without calibration due to the individual phase delay of the electronics involved. Since only relative phase delays between measurements could be analysed, we used only the amplitude in the retrieval of α_{M} but not the phase.

Fig. 5 shows a typical TTAOS simulation (brown trace) as a function of the average droplet radius $\bar{r}$ and the average real part of the refractive index $\bar{n}_{\mathrm{r}}$. The cyan trace visualises how a typical MMS signal amplitude looks like when a droplet shrinks over time from $\bar{r}$ = 1.7 to 1.5 μm. Double-peak features appear in the MMS signals in the vicinity of the maxima of Mie resonances (maxima brown trace). A more comprehensive description of the MMS signal generation is given in ref. 62.

Fig. 4(a) shows an experimentally recorded MMS amplitude trace that is compared to four simulated MMS amplitudes for different values of α_{M} between 0.01–1. At smaller droplet radii, $\mathrm{MMS}_{\mathrm{A}}^{\mathrm{exp}}$ overlaps best with the orange trace. Towards higher radii, $\mathrm{MMS}_{\mathrm{A}}^{\mathrm{exp}}$ agrees better with the purple trace, indicating a reduction of α_{M} with increasing radius. This is due to the fact that in our experiments larger droplets reach equilibrium at higher average particle temperatures.

The double-peak features are the essential features for the determination of the mass accommodation coefficient. α_{M} (fit parameter) is determined from a fit of the calculated MMS trace (eqn (9); light blue trace in Fig. 4(b)) of one double-peak to the experimental trace (eqn (2), dark blue trace in Fig. 4(b)) by minimising the normalised sum of squared residuals SSR (for more information, see ESI†):

$$\mathrm{SSR} = \frac{\sum\left(\mathrm{MMS}_{\mathrm{A}}^{\mathrm{sim,norm}} - \mathrm{MMS}_{\mathrm{A}}^{\mathrm{exp,norm}}\right)^2}{\sum \mathrm{MMS}_{\mathrm{A}}^{\mathrm{exp,norm}}} \tag{11}$$

Fig. 4(b) compares a typical experimental MMS trace (dark blue) with a calculated trace (light blue). The two traces show excellent agreement. For completeness, the red and the magenta trace show the experimental ($\mathrm{MMS}_{\phi}^{\mathrm{exp}}$) and calculated MMS phase ($\mathrm{MMS}_{\phi}^{\mathrm{sim}}$, Eqn 10), respectively. Note that the phase was not used to determine α_{M}. Considering that no calibration was performed on the phase measurements, the agreement between the simulated and experimental phase is very good.

4 Results and discussion

The MMS signal responses for 176 individual droplets were recorded for droplet sizes in the range between $\bar{r}$ = 0.7 and 2 μm at different temperatures between $\bar{T}$ = 21 °C and 26 °C and different RHs between 8 and 96% RH (1.5% relative error). The RH determines the droplet composition.[50,51] The examined RH range corresponds to water mole fractions x_{mol} between 0.1 and 0.93, covering a broad range of different droplet compositions from almost pure TREG droplets ($<2\%$ water by volume) to water-rich droplets ($<60\%$ water by volume), and we exclude data obtained above $x_{\text{mol}} = 0.78$ ($\gtrsim 35\%$ water by volume) because of measurement artefacts (see below). We note that the presented results cannot be used to obtain α_M for water on water. In total, more than 3100 MMS double-peak features (Fig. 5) were fitted to retrieve α_M over this x_{mol} and $\bar{T}$ range.

In the following, we indicate the average (averaged over a modulation cycle) water mole fraction x_{mol}, the average water volume fraction x_{vol} and the average droplet temperature T of the top layer of the droplet (thickness ≈ 50 nm), obtained from the MHM-PA simulations. Even though all these values deviate only by a few percent from the values averaged over the whole droplet, they represent conditions close to the surface best.

4.1 Observed trends

Fig. 6(a) and (b) show α_M of aqueous TREG droplets as a function of $\overline{\text{T}}$ (colour code) and x_{mol} (left) and x_{vol} (right), respectively. The volume fraction was calculated using the densities of bulk TREG and water.[50,63] Two general trends are visible:

(i) α_M has a comparatively high value around 0.1 for almost pure TREG droplets ($x_{\text{mol}} \approx 0.1$, $x_{\text{vol}} \approx 0.015$). With increasing water content, α_M then quickly decreases, reaching minimum values around 0.005 at $x_{\text{mol}} \approx 0.38$ ($x_{\text{vol}} \approx 0.075$). A further increase of the water content in the droplet reverses the behaviour and results in a temperature-dependent increase of α_M, again reaching a value of ≈ 0.1 for water rich droplets with $x_{\text{mol}} \approx 0.6$ ($x_{\text{vol}} \approx 0.17$) at the lowest temperatures. Above $x_{\text{mol}} \approx 0.78$ ($x_{\text{vol}} \approx 0.33$), α_M appears to slightly decrease again. We believe, however, that this apparent decrease is a measurement artefact. These data points were retrieved from measurements at very high RH ($>90\%$). At such high relative humidities, condensation of water on the cell windows can easily build up. This can cause distortions of the IR laser beam resulting in a reduction of the overall light intensity, and hence a reduced MMS response and thus α_M values that are slightly too low.

(ii) A temperature-dependence that is correlated with the water content in the droplet. For mole fractions between 0.38 and 0.6 and the lowest temperatures, the α_M values show a distinct increase with increasing water content. The extent of this increase decreases as the temperature rises, and disappears for the highest temperatures. The data also show that α_M does not strongly depend on the water concentration above $x_{\text{mol}} \approx 0.6$. At mole fractions below $x_{\text{mol}} \approx 0.38$ ($x_{\text{vol}} \approx 0.075$), where α_M is minimal, α_M is essentially temperature independent – the data points recorded at different temperatures more or less overlap here, except for outliers.

4.2 Unexpected concentration dependence

How can these two trends be explained? The pronounced minimum in α_M at intermediate water concentrations ($x_{\text{mol}} \approx 0.38$) is unexpected and seems rather unusual (case (i) in Section 4.1). At first sight, one would expect to observe a more or less monotonous trend of α_M with increasing water content because water and TREG are fully miscible. The most likely behaviour would be an increase in α_M with changing water content, simply because water is expected to interact more strongly with water than with TREG. However, for the aqueous TREG droplets this trend is only found above $x_{\text{mol}} \approx 0.38$ ($x_{\text{vol}} \approx 0.075$), but not below that value. We observed the same trend also for water accommodation on aqueous tetraethylene glycol (TEG) droplets above $x_{\text{mol}} \approx 0.5$.[7,43] This more or less expected trend can be explained by a continuous increase of the number of H_2O molecules at the droplet's surface and thus likely an increase of free OH groups of H_2O surface molecules that facilitate water accommodation at the surface. That α_M reaches a minimum at $x_{\text{mol}} \approx 0.38$, would indicate that at this composition only a few free OH groups are available to accommodate incoming H_2O gas phase molecules because the TREG

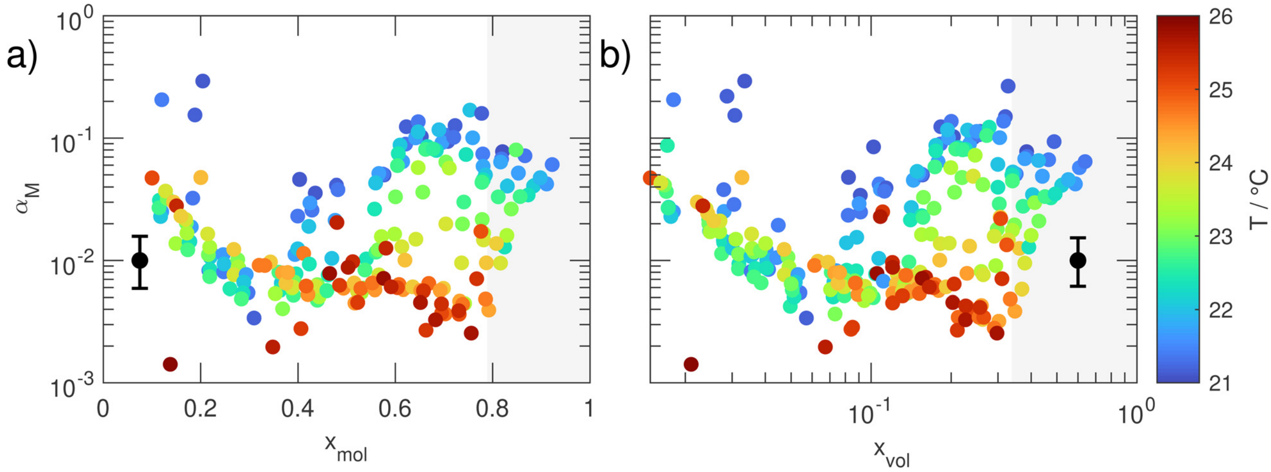

Fig. 6 Mass accommodation coefficient α_M as a function of (a) the water mole fraction x_{mol} and (b) the water volume fraction x_{vol}. The black marker in the lower left/right of the respective panels indicates the mean uncertainty in α_M. The individual uncertainties are tabulated in the data repository to this article. The data points in the grey shaded area are referred to as excluded data points because their values are likely influenced by measurement artefacts (see text). The uncertainty in temperature is typically below 0.15 °C and always below 0.5 °C.

and H_2O molecules at the surface form a common more or less saturated hydrogen-bond network. When x_{mol} is reduced below ≈ 0.38, α_M again increases pronouncedly. The increasing lack of water molecules in this concentration range renders the formation of a saturated TREG–H_2O hydrogen-bond network less and less likely. This in turn could result in an increased number of free OH groups from TREG at the droplet's surface, which again would facilitate water accommodation from the gas phase and thus result in an increased α_M value. At the lowest water mole fraction, α_M can be interpreted as water mass accommodation on an almost pure TREG surface.

The observed minimum of α_M at $x_{mol} \approx 0.38$ seems consistent with a special behaviour previously observed for other quantities. Begum *et al.* found a pronounced maximum in excess viscosity at $x_{mol} \approx 0.3–0.4$: they argue that this might be caused by a strengthening of the hydrogen bond network in the water–TREG solution at this composition.[64] Klimaszewski *et al.* measured the speed of sound in aqueous TREG solutions and found a distinct kink in their data at $x_{mol} \approx 0.3–0.4$. They proposed that this could be caused by progressive replacement of water–water bonds with newly formed water–TREG bonds when going from water rich solutions to $x_{mol} \approx 0.3–0.4$.[65] Their data also suggest that the temperature dependence for the excess sound velocity almost vanishes below $x_{mol} \approx 0.3$ (see the following subsection). Both the viscosity and speed of sound are related to the mutual diffusion coefficient of aqueous TREG, which can influence the net water mass accommodation.[27,33]

Shinyashiki *et al.* and Sudo *et al.* performed broadband dielectric measurements on aq. TREG and other ethylene glycol oligomers.[66–68] They drew conclusions about the molecular interactions and the cooperative motion of water and solute molecules. They proposed that the water molecules in mixtures with high water content have the ability to move cooperatively, which is primarily facilitated by the formation of hydrogen bonds and small clusters with surrounding water molecules. Shinyashiki *et al.* argued that ethylene glycol and diethylene glycol are small enough to efficiently form clusters with water molecules, but TREG molecules are already too large to facilitate cooperative motions, and actually act as a constraint in the water binding network.[66,68] This might explain why the values of α_M at higher water content ($x_{mol} \approx 0.4–0.8$, $x_{vol} \approx 0.08–0.33$) are lower than the value of α_M of water on pure water, which is assumed to be >0.6.[9,26,27,29] For aqueous TREG mixtures with lower water content, by contrast, they argue that the water molecules lack the ability to move cooperatively because the large TREG molecules impose a global geometric constraint on the movement of the water molecules. In this case, the (cooperative) motion of TREG molecules becomes important for transport inside the liquid.[67] These dynamics and associated structural changes might support our explanation regarding the formation of a minimum in α_M provided above.

Note that the studies mentioned above consider bulk mixtures, and can only serve as indications of how the surface and near-surface structure may be organised. The molecular interpretations suggested in this article and in the referenced publications are hypothetical scenarios that could explain the unusual concentration dependence of α_M. Molecular dynamics simulations (MD) of water accommodation at surfaces might provide more insight into the molecular origin. What is crucial, however, is that these simulations apply to the specific system under consideration. To the best of our knowledge, there are no such studies on the accommodation of water on TREG, nor are there any other simulations representative (*e.g.* (poly-)ethylene glycol water surfaces) of the system studied here. MD simulations for water accommodation are available for surfactants or molecules with low solubility in water,[13,14,61,69–72] which however, differ greatly from our water TREG system.

4.3 Temperature dependence

The temperature trend (see (ii) in Section 4.1) and its correlation with the water content are again visualised in Fig. 7 in a slightly different way than in Fig. 6. Fig. 7 shows α_M as a function of temperature and x_{vol} (dichotomous colour code). For water contents below the critical value where α_M reaches a minimum ($x_{vol} < 0.075$; light brown to black colours), α_M is temperature independent within uncertainties. For larger water contents (light to dark green), by contrast, an inverse temperature dependence is visible for the higher volume fractions (darker green) at all temperatures and for the lower volume fractions (lighter green) at the lower temperatures (see also Fig. 8 and Table 1).

To analyse the temperature dependence, Davidovits *et al.*[48] proposed to describe mass accommodation as a two-step process, resulting in a Gibbs energy of the transition state

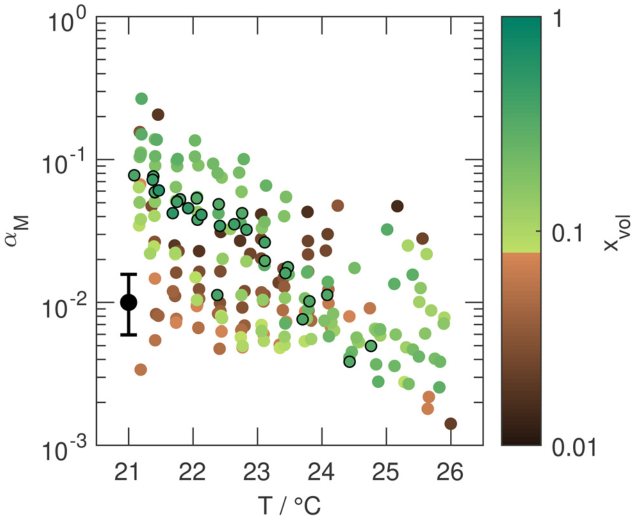

Fig. 7 Mass accommodation coefficient α_M as a function of the temperature T of the surface layer of the droplet. The water volume fractions below the critical value x_{vol} = 0.075 are indicated by brown to black colours. The water volume fractions above the critical value x_{vol} = 0.075 are indicated by green colours. The black marker in the lower left illustrates the mean uncertainty in α_M. The individual uncertainties are tabulated in the data repository to this article. The data points with the black borders are referred to as excluded data points because their values are likely influence by measurement artefacts (see text). The uncertainty in temperature is typically below 0.15 °C and always below 0.5 °C.

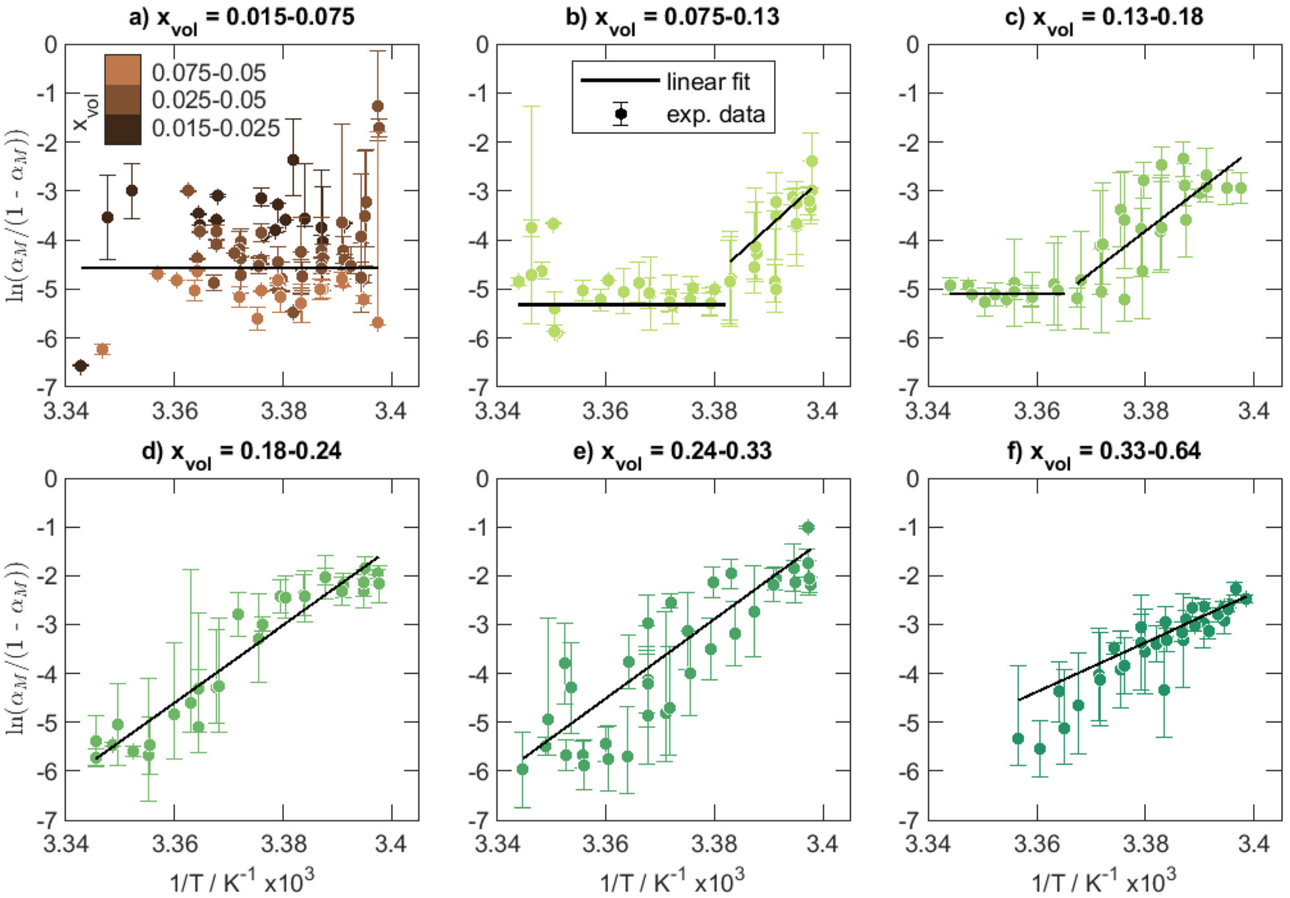

Fig. 8 Arrhenius type plot of α_M according to eqn (16) for six defined classes of volume fraction. To guide the eye, the colours of the data points in the respective panels are chosen according to the colour scale in Fig. 7. Panel (a) shows the class below and panels (b) to (e) show the classes above the critical water concentration of x_{vol} = 0.075 (x_{mol} = 0.38). The black lines show the linear fits according to eqn (16). Panel (f) shows the class of excluded data points (measurement artefacts).

between the gas phase and the solvated molecule $\Delta G_{obs} = \Delta H_{obs} - T\Delta S_{obs}$ (ESI,† Section 2 and Fig. S4). The first step is the adsorption of a gas phase molecule at the surface (k_{ads}) and the second step is either the solvation of this molecule (k_{sol}) or the desorption of the molecule back into the gas phase (k_{des}).

$$[\mathrm{H_2O}]_g \underset{k_{des}}{\overset{k_{ads}}{\rightleftharpoons}} [\mathrm{H_2O}]_s \xrightarrow{k_{sol}} [\mathrm{H_2O}]_l \qquad (12)$$

The subscripts g indicate gas phase water molecules, s surface adsorbed molecules and l liquid phase molecules. Assuming that the collision rate of gas phase water molecules with the surface is equal to the adsorption rate, the mass accommodation coefficient is

$$\alpha_M = \frac{k_{sol}[\mathrm{H_2O}]_s}{k_{ads}[\mathrm{H_2O}]_g}. \qquad (13)$$

Table 1 Activation enthalpy ΔH_{obs} and entropy ΔS_{obs} for mass accommodation of water on aqueous TREG droplets from Arrhenius type fits according to eqn (16). Classes (a) to (f) represent the same concentration classes as in Fig. 8. Note that (f) corresponds to the class of excluded data points (measurement artefact). The indicated uncertainty represents the 95% confidence interval of the applied linear model

Class	T-range °C	x_{vol}	x_{mol}	ΔH_{obs} kJ mol^{-1}	ΔS_{obs} J mol^{-1} K^{-1}	ΔG_{obs} (21 °C) kJ mol^{-1}	ΔG_{obs} (26 °C) kJ mol^{-1}
(a)	21–26	0.015–0.075	0.1–0.38	0	−38 ± 5	11.2	11.4
(b)	21–22.5	0.075–0.13	0.38–0.50	−834 ± 230	−2858 ± 782	6.8	—
	22.5–26	0.075–0.13	0.38–0.50	0	−44 ± 5	—	13.2
(c)	21–24	0.13–0.18	0.50–0.62	−706 ± 70	−2417 ± 235	5.3	—
	24–26	0.13–0.18	0.50–0.62	0	−42 ± 1	—	12.7
(d)	21–26	0.18–0.24	0.62–0.70	−661 ± 21	−2260 ± 72	3.7	14.9
(e)	21–26	0.24–0.33	0.70–0.78	−674 ± 27	−2302 ± 90	3.2	14.7
(f)	21–26	0.33–0.64	0.78–93	−420 ± 40	−1447 ± 136	5.8	13.0

Note that this assumption is in agreement with ref. 48 and 73, and also consistent with molecular dynamics simulations.[14,74] Assuming quasi-stationarity for surface adsorbed molecules

$$\frac{[\mathrm{H_2O}]_\mathrm{s}}{\mathrm{d}t} = k_\mathrm{ads}[\mathrm{H_2O}]_\mathrm{g} - k_\mathrm{des}[\mathrm{H_2O}]_\mathrm{s} - k_\mathrm{sol}[\mathrm{H_2O}]_\mathrm{s} \approx 0, \tag{14}$$

this model results in the following relation between α_M and ΔG_obs:

$$\frac{\alpha_\mathrm{M}}{1-\alpha_\mathrm{M}} = \frac{k_\mathrm{sol}}{k_\mathrm{des}} = \exp\left(\frac{-\Delta G_\mathrm{obs}}{RT}\right) \tag{15}$$

This provides the following linear inverse temperature dependence of the logarithm of $\frac{\alpha_\mathrm{M}}{1-\alpha_\mathrm{M}}$:

$$\ln\frac{\alpha_\mathrm{M}}{1-\alpha_\mathrm{M}} = -\frac{\Delta H_\mathrm{obs}}{R}\frac{1}{T} + \frac{\Delta S_\mathrm{obs}}{R} \tag{16}$$

with the activation enthalpy and entropy ΔH_obs and ΔS_obs, respectively.

ΔH_obs and ΔS_obs were retrieved from the experimental data in Fig. 7 using eqn (16). To account for the correlation between temperature dependence and water content, we first divided the data in six classes with similar water content, with one class below the critical $x_\mathrm{vol} < 0.075$ where α_M is minimal (Fig. 8(a)) and five classes above this threshold (Fig. 8(b)–(f)). Table 1 lists for all classes the enthalpy of activation ΔH_obs, the entropy of activation ΔS_obs, and the activation Gibbs energies ΔG_obs for the two limiting temperatures of the experiment.

The data in Fig. 8(a) does not show indications for a systematic temperature dependence, suggesting that the formation of the transition state on TREG-rich surfaces is enthalpically neutral ($\Delta H_\mathrm{obs} \approx 0$, Table 1 (a)) within the uncertainty. The energy gain by forming new interactions with the incoming gas phase water molecule is more or less balanced by the loss of energy that is required to disturb the surface. For $\Delta H_\mathrm{obs} \approx 0$, ΔS_obs is negative, indicating that the formation of the transition state is entropically hindered. The reduction in entropy can be rationalised by the fact that the number of degrees of freedom reduces as a molecule transitions from the gas phase to a more restricted surface bound molecule. The value of ΔS_obs indicated in Table 1 (a) corresponds to the value averaged over the entire concentration range below the critical concentration $x_\mathrm{vol} <$ 0.075, assuming that $\Delta H_\mathrm{obs} = 0$. This averaging neglects any concentration dependence. To identify potential concentration trends, we grouped the data into three subclasses as indicated by the colour scheme in panel (a). We calculated ΔS_obs at different concentrations for $\Delta H_\mathrm{obs} = 0$, and we found that ΔS_obs becomes more negative with increasing water content (by less than factor of two). This increase in the entropic barrier might explain the observed decrease in α_M for increasing water content in the region $x_\mathrm{vol} < 0.075$ (Fig. 6), suggesting that a higher content of surface water increasingly hinders the formation of the transition state in this concentration range. However, because of the measurement uncertainties and because ΔS_obs and ΔH_obs are correlated, the interpretation that the observed decrease in α_M is purely entropic is only tentative.

The next two concentration classes in Fig. 8(b) and (c) show a strong temperature dependence of ΔH_obs which is given by the negative of the slope of $\ln\frac{\alpha_\mathrm{M}}{1-\alpha_\mathrm{M}}$ with respect to the inverse temperature (Gibbs–Helmholtz equation). Within the accuracy of our measurements, we can distinguish two regions: above a certain temperature (22.5 °C and 24 °C in Fig. 8(b) and (c), respectively) $\Delta H_\mathrm{obs} \approx 0$. Below this temperature, ΔH_obs is finite and we approximate it as temperature independent (approximately linear behaviour in Fig. 8(b) and (c)). The corresponding values of ΔH_obs and ΔS_obs resulting from eqn (16) are given in Table 1. The formation of the transition state is entropically hindered (negative activation entropy) for both concentration classes, and either enthalpically neutral (no activation enthalpy) or enthalpically favoured (negative activation enthalpy) depending on the temperature. Interestingly, in the concentration range represented by Fig. 8(b) and (c), the temperature region where $\Delta H_\mathrm{obs} = 0$ correlates with an α_M that is approximately concentration independent (Fig. 6), while the temperature region where ΔH_obs is finite correlates with the range where α_M increases linearly with increasing water content.

In the concentration range x_vol = 0.18–0.33, α_M strongly depends on the temperature but is essentially independent of the water content (Fig. 6). This concentration range corresponds to the two concentration classes shown in Fig. 8(d) and (e). As for the lower temperatures in classes (b) and (c), an inverse temperature dependence is observed, which again can be well approximated by a temperature-independent, finite ΔH_obs. The data in Table 1 (d) to (e) show that in this concentration range the formation of the transition state is enthalpically favoured and entropically hindered. The fact that the water accommodation is enthalpically favoured is not surprising for systems that are considered to be miscible, such as TREG–water solutions. As mentioned further above, the apparent slight decrease of α_M for the highest water concentration (x_vol = 0.33–0.64, Fig. 6) is likely not real but caused by a measurement artefact. Thus, we also anticipate this measurement artefact to be the reason for the apparent change of the values of ΔH_obs and ΔS_obs (Fig. 8(f) and Table 1 (f)) compared with those in the classes (d) and (e).

The (non-zero) ΔH_obs values, the ΔS_obs values and ΔG_obs values in the classes (b) to (e) are essentially indistinguishable within uncertainties (Table 1 (b)–(e)). This hints that there is no pronounced concentration-dependence of ΔH_obs and ΔS_obs above the critical concentration $x_\mathrm{vol} > 0.075$ for the lower temperatures where ΔH_obs is non-zero. Potentially, there might be a slight trend towards less negative ΔH_obs and ΔS_obs values with increasing water content (Table 1 (b)–(e)), but again this is difficult to say given the quality of the data. The stability in the thermodynamic quantities with respect to the concentration might be related to the almost constant surface tension of aqueous TREG at water concentrations below $x_\mathrm{vol} < 0.33$ ($x_\mathrm{mol} \approx 0.8$), which changes by less than 8%.[50]

5 Conclusion

It has previously been reported that α_M of water on aqueous systems containing surface-active or immiscible compounds show a complex dependence of α_M on the composition and temperature. The present work reveals that pronounced non-trivial dependencies on composition and temperature can also occur for water miscible compounds (here TREG). This behaviour was rather unexpected. This result might be relevant for questions concerning aerosolised pharmaceutics as well as cloud activation by atmospheric aerosols, *e.g.* hinting at a generally very sensitive and complex temperature and concentration dependence of the cloud activation potential of aerosols.

We investigated the behaviour of α_M on aqueous TREG droplets from almost pure TREG droplets to almost pure water droplets over a comparatively small temperature range from 21 °C to 26 °C. Single optically-trapped droplets were excited by an intensity-modulated infrared laser resulting in minor oscillatory changes of the droplet radius, composition, and Mie scattering pattern (MMS). α_M was retrieved from the analysis of the MMS patterns with a kinetic multilayer model.

We observed a composition-dependent variation of α_M by almost two orders of magnitude, covering the range from less than 0.005 to more than 0.1. Surprisingly, for the lower temperatures the values of α_M lie close to 0.1 for TREG-rich and water-rich droplets, while the minimum value of α_M is reached at intermediate concentrations (water mole fractions of 0.38). The minimum of α_M might be explained by the formation of a more or less saturated hydrogen-bond network between TREG and water forming at the surface at intermediate concentrations, minimising the sites (*e.g.* free OH groups) where gas phase water molecules can accommodate. The high values of α_M for TREG-rich and water-rich droplets could be the result of an increase in the number of free OH-groups at the surface facilitating water accommodation from the gas phase. At concentrations below the minimum of α_M, α_M is essentially temperature independent. Above the minimum, however, α_M decreases systematically from 0.1 to 0.005 with increasing temperature.

An Arrhenius type analysis reveals that the formation of the transition state is entropically hindered at all conditions studied, in agreement with the fact that the number of degrees of freedom reduce when a molecule transitions from the gas phase to a more restricted surface-bound molecule. Our analysis suggests that the formation of the transition state is enthalpically neutral at concentrations below the minimum of α_M and enthalpically favoured at higher water concentrations. In the intermediate concentration range, the enthalpy of activation is strongly temperature-dependent. These findings underscore the sensitivity of α_M to moderate changes in conditions even for miscible systems. The present results for the supposedly simple, miscible TREG–water system further highlight the complexity of the interplay between different factors governing mass accommodation.

Data availability

The data repository related to this article can be found at **https://doi.org/10.3929/ethz-b-000673390**.

Conflicts of interest

There are no conflicts to declare.

Acknowledgements

The authors thank Dr. Tanya L. Myers from the Pacific Northwest National Laboratory for providing the complex refractive index data of TREG, Dr. Pablo Corral Arroyo who developed the original version of the MHM-PA model, and Markus Steger and David Stapfer for technical support. This work was financially supported by the Swiss National Science Foundation (SNSF grant. no. 200020-200306) and ETH Zurich. The authors declare no competing financial interest.

Notes and references

1 J. C. Maxwell, *Phil. Trans. Royal Society*, 1859, **1**, 49–88.
2 P. Davidovits, C. E. Kolb, L. R. Williams, J. T. Jayne and D. R. Worsnop, *Chem. Rev.*, 2006, **106**, 1323–1354.
3 P. Davidovits, C. E. Kolb, L. R. Williams, J. T. Jayne and D. R. Worsnop, *Chem. Rev.*, 2011, **111**, PR76–PR109.
4 E. Davis, *Atmos. Res.*, 2006, **82**, 561–578.
5 C. E. Kolb, R. A. Cox, J. P. D. Abbatt, M. Ammann, E. J. Davis, D. J. Donaldson, B. C. Garrett, C. George, P. T. Griffiths, D. R. Hanson, M. Kulmala, G. McFiggans, U. Pöschl, I. Riipinen, M. J. Rossi, Y. Rudich, P. E. Wagner, P. M. Winkler, D. R. Worsnop and C. D. O'Dowd, *Atmos. Chem. Phys.*, 2010, **10**, 10561–10605.
6 J. P. D. Abbatt, A. K. Y. Lee and J. A. Thornton, *Chem. Soc. Rev.*, 2012, **41**, 6555–6581.
7 M. E. Diveky, M. J. Gleichweit, S. Roy and R. Signorell, *J. Phys. Chem. A*, 2021, **125**, 3528–3548.
8 A. H. Persad and C. A. Ward, *Chem. Rev.*, 2016, **116**, 7727–7767.
9 A. Laaksonen, T. Vesala, M. Kulmala, P. M. Winkler and P. E. Wagner, *Atmos. Chem. Phys.*, 2005, **5**, 461–464.
10 A. P. Kryukov and V. Y. Levashov, *Int. J. Heat Mass Transfer*, 2011, **54**, 3042–3048.
11 A. Morita, M. Sugiyama, H. Kameda, S. Koda and D. R. Hanson, *J. Phys. Chem. B*, 2004, **108**, 9111–9120.
12 A. Morita and B. C. Garrett, *Fluid Dyn. Res.*, 2008, **40**, 459.
13 W. Li, C. Y. Pak, X. Wang and Y.-L. S. Tse, *J. Phys. Chem. C*, 2019, **123**, 18924–18931.
14 M. von Domaros, P. S. J. Lakey, M. Shiraiwa and D. J. Tobias, *J. Phys. Chem. B*, 2020, **124**, 3836–3843.
15 X. Li and I. C. Bourg, *Environ. Sci. Technol.*, 2023, **57**, 13092–13103.
16 S. M. Johansson, J. Lovrić, X. Kong, E. S. Thomson, P. Papagiannakopoulos, S. Briquez, C. Toubin and

J. B. C. Pettersson, *Phys. Chem. Chem. Phys.*, 2019, **21**, 1141–1151.

17 J. Julin, P. M. Winkler, N. M. Donahue, P. E. Wagner and I. Riipinen, *Environ. Sci. Technol.*, 2014, **48**, 12083–12089.

18 P. Varilly and D. Chandler, *J. Phys. Chem. B*, 2013, **117**, 1419–1428.

19 U. Pöschl, Y. Rudich and M. Ammann, *Atmos. Chem. Phys.*, 2007, **7**, 5989–6023.

20 G. M. Nathanson, P. Davidovits, D. R. Worsnop and C. E. Kolb, *J. Phys. Chem.*, 1996, **100**, 13007–13020.

21 M. Shiraiwa, C. Pfrang and U. Pöschl, *Atmos. Chem. Phys.*, 2010, **10**, 3673–3691.

22 M. Shiraiwa and U. Pöschl, *Atmos. Chem. Phys.*, 2021, **21**, 1565–1580.

23 M. Kulmala and P. E. Wagner, *J. Aerosol Sci.*, 2001, **32**, 833–841.

24 R. Marek and J. Straub, *Int. J. Heat Mass Transfer*, 2001, **44**, 39–53.

25 I. Eames, N. Marr and H. Sabir, *Int. J. Heat Mass Transfer*, 1997, **40**, 2963–2973.

26 D. Jakubczyk, M. Zientara, K. Kolwas and M. Kolwas, *J. Atmos. Sci.*, 2007, **64**, 996–1004.

27 R. E. H. Miles, J. P. Reid and I. Riipinen, *J. Phys. Chem. A*, 2012, **116**, 10810–10825.

28 P. Davidovits, D. R. Worsnop, J. T. Jayne, C. E. Kolb, P. Winkler, A. Vrtala, P. E. Wagner, M. Kulmala, K. E. J. Lehtinen, T. Vesala and M. Mozurkewich, *Geophys. Res. Lett.*, 2004, **31**, L22111.

29 J. D. Smith, C. D. Cappa, W. S. Drisdell, R. C. Cohen and R. J. Saykally, *J. Am. Chem. Soc.*, 2006, **128**, 12892–12898.

30 M. E. Diveky, S. Roy, J. W. Cremer, G. David and R. Signorell, *Phys. Chem. Chem. Phys.*, 2019, **21**, 4721–4731.

31 S. T. Govoni and G. M. Nathanson, *J. Am. Chem. Soc.*, 1994, **116**, 779–780.

32 G. M. Nathanson, *Annu. Rev. Phys. Chem.*, 2004, **55**, 231–255.

33 R. E. H. Miles, J. F. Davies and J. P. Reid, *Phys. Chem. Chem. Phys.*, 2016, **18**, 19847–19858.

34 J. F. Davies, R. E. H. Miles, A. E. Haddrell and J. P. Reid, *Proc. Natl. Acad. Sci. U. S. A.*, 2013, **110**, 8807–8812.

35 J. M. Langridge, M. S. Richardson, D. A. Lack, C. A. Brock and D. M. Murphy, *Aerosol Sci. Technol.*, 2013, **47**, 1163–1173.

36 X. Kong, E. S. Thomson, P. Papagiannakopoulos, S. M. Johansson and J. B. C. Pettersson, *J. Phys. Chem. B*, 2014, **118**, 13378–13386.

37 W. Lester Jr, S. Kaye, O. Robertson and E. W. Dunklin, *Am. J. Public Health*, 1950, **40**, 813–820.

38 P. Gandhidasan, *Energy Sources*, 2003, **25**, 189–201.

39 B. Ballantyne and W. M. Snellings, *J. Appl. Toxicol.*, 2007, **27**, 291–299.

40 X. Guo, T. Ehindero, C. Lau and R. Zhao, *Indoor Air*, 2022, **32**, e13100.

41 C. Rainey, J. Shifflett, J. Goodpaster and D. Bezabeh, *Nicotine Tob. Res.*, 2013, **25**, 576–585.

42 J. W. Cremer, K. M. Thaler, C. Haisch and R. Signorell, *Nat. Commun.*, 2016, **7**, 10941.

43 S. Roy, M. E. Diveky and R. Signorell, *J. Phys. Chem. C*, 2020, **124**, 2481–2489.

44 S. Roy, M. E. Diveky and R. Signorell, *J. Phys. Chem. C*, 2020, **124**, 17848–17849.

45 M. E. Diveky, S. Roy, G. David, J. W. Cremer and R. Signorell, *Photoacoustics*, 2020, **18**, 100170.

46 M. E. Diveky, S. Roy, J. W. Cremer, G. David and R. Signorell, *Phys. Chem. Chem. Phys.*, 2020, **22**, 15770–15771.

47 P. Corral Arroyo, M. J. Gleichweit, M. E. Diveky and R. Signorell, *Aerosol Sci. Technol.*, 2023, **57**, 742–757.

48 P. Davidovits, J. T. Jayne, S. X. Duan, D. R. Worsnop, M. S. Zahniser and C. E. Kolb, *J. Phys. Chem.*, 1991, **95**, 6337–6340.

49 M. E. Diveky, M. J. Gleichweit, S. Roy, E. Bartalucci and R. Signorell, Proc. SPIE 11463, OTOM XVII, 2020, pp. 115-131.

50 The Dow Chemical Company, Triethylene Glycol, Dow tech-report XXX-0207X CRCG, 2007.

51 U. K. Krieger, F. Siegrist, C. Marcolli, E. U. Emanuelsson, F. M. Gøbel, M. Bilde, A. Marsh, J. P. Reid, A. J. Huisman, I. Riipinen, N. Hyttinen, N. Myllys, T. Kurtén, T. Bannan, C. J. Percival and D. Topping, *Atmos. Meas. Tech.*, 2018, **11**, 49–63.

52 C. F. Bohren and D. R. Huffman, *Absorption and Scattering of Light by Small Particles*, John Wiley & Sons, Ltd, 1998.

53 G. David, O. Reich, M. E. Divéky, S. Roy, E. A. Parmentier, J. W. Cremer, K. Esat and R. Signorell, Proc. SPIE11083, OTOM XVI, 2019, p. 1108322.

54 M. Shiraiwa, C. Pfrang, T. Koop and U. Pöschl, *Atmos. Chem. Phys.*, 2012, **12**, 2777–2794.

55 M. Kulmala, T. Vesala and P. E. Wagner, *Proc. R. Soc. London, Ser. A*, 1993, **441**, 589–605.

56 D. M. Murphy, *Aerosol Sci. Technol.*, 2009, **43**, 356–363.

57 P. M. Winkler, A. Vrtala, R. Rudolf, P. E. Wagner, I. Riipinen, T. Vesala, K. E. J. Lehtinen, Y. Viisanen and M. Kulmala, *J. Geophys. Res.*, 2006, **111**, D19202.

58 N. A. Fuchs and A. G. Sutugin, *Topics in Current Aerosol Research*, Pergamon, 1971, vol. 2, ch. Properties of HDAs, pp.29–37.

59 Y. Q. Li, P. Davidovits, C. E. Kolb and D. R. Worsnop, *J. Phys. Chem. A*, 2001, **105**, 10627–10634.

60 I. Riipinen, B. Svenningsson, M. Bilde, A. Gaman, K. Lehtinen and M. Kulmala, *Atmos. Res.*, 2006, **82**, 579–590.

61 P. S. J. Lakey, B. E. Cummings, M. S. Waring, G. C. Morrison and M. Shiraiwa, *Environ. Sci.: Processes Impacts*, 2023, **25**, 1464–1478.

62 M. J. Gleichweit, M. Azizbaig Mohajer, D. Borgeaud, M. E. Diveky, G. David and R. Signorell, Proc. SPIE 12198, OTOM XIX 2022, p. 1219805.

63 J. Rumble, *CRC Handbook of Chemistry and Physics*, CRC Press/Taylor & Francis Group, 99th edn, 2018.

64 S. K. Begum, R. J. Clarke, M. S. Ahmed, S. Begum and M. A. Saleh, *J. Mol. Liq.*, 2013, **177**, 11–18.

65 K. Klimaszewski, E. Stronka-Lewkowska, K. Abramczyk and A. Bald, *J. Chem. Thermodyn.*, 2015, **89**, 212–222.

66 N. Shinyashiki, S. Sudo, W. Abe and S. Yagihara, *J. Chem. Phys.*, 1998, **109**, 9843–9847.

67 S. Sudo, N. Shinyashiki, Y. Arima and S. Yagihara, *Phys. Rev. E: Stat., Nonlinear, Soft Matter Phys.*, 2008, **78**, 011501.

68 S. Sudo, S. Tsubotani, M. Shimomura, N. Shinyashiki and S. Yagihara, *J. Chem. Phys.*, 2004, **121**, 7332–7340.

69 P. Chakraborty and M. R. Zachariah, *J. Phys. Chem. A*, 2008, **112**, 966–972.

70 X. Ma, P. Chakraborty, B. J. Henz and M. R. Zachariah, *Phys. Chem. Chem. Phys.*, 2011, **13**, 9374–9384.

71 S. Takahama and L. M. Russell, *J. Geophys. Res.*, 2011, **116**, D02203.

72 G. Ergin and S. Takahama, *J. Phys. Chem. A*, 2016, **120**, 2885–2893.

73 J. T. Jayne, S. X. Duan, P. Davidovits, D. R. Worsnop, M. S. Zahniser and C. E. Kolb, *J. Phys. Chem.*, 1991, **95**, 6329–6336.

74 B. C. Garrett, G. K. Schenter and A. Morita, *Chem. Rev.*, 2006, **106**, 1355–1374.